Supplementary Information

Reconfiguration and activation induced by characteristic migration of transition metal-ions between interfaces of high-entropy oxygen evolution catalysts

Wei Zuo,[a,b] Zhenhang Xu,[b] Jun Qian,[a] Gongzhen Cheng,[b] and Pingping Zhao[a]

[a.] *School of Nursing, Wuhan University, Wuhan, Hubei 430072, P. R. China. Tel.: +86 2768778433. E-mail: ppzhao@whu.edu.cn*

[b.] *College of Chemistry and Molecular Sciences, Wuhan University, Wuhan, Hubei 430072, P. R. China. E-mail: gzcheng@whu.edu.cn*

S1. Experimental Details

S1.1. Synthesis of the Ni-MOF

At room temperature, 0.8g nickel nitrate hexahydrate [$Ni(NO_3)_2 \cdot 6H_2O$] was completely dissolved in 60 ml ethanol, deionized water and N, N-dimethylformamide mixed solvent, mixing ratio is V_{EtOH}: V_{H2O}: V_{DMF} = 1:1:1. 0.3g of 1,3,5-Benzenetricarboxylic acid ($C_9H_6O_6$) and 2g PVP (M.W. = 40 000) was added to the mixed solvent in magnetic agitation in batches, and the above solution was treated with ultrasonic wave for 30 min, so that the solid substance was fully dissolved and a uniform green transparent solution was formed. Transfer the above solution to a 50 ml Teflon reactor and react in an oven at 200 ° C for 24 hours. At the end of the reaction, the synthesized sample is washed several times with ethanol and deionized water to remove unreacted chemicals and residual solvents. The washed solution was centrifuged, the precipitate was collected, and then dried for 12 h to obtain Ni-MOF samples.

S1.2. Synthesis of the ZIF-67 (Co)

Dissolve 3.6 g cobalt nitrate hexahydrate [$Co(NO_3)_2 \cdot 6H_2O$] in 250 ml methanol at room temperature, configured as solution A. Similarly, 8.13 g 2-methylimidazole was dissolved in 250 ml methanol, configured as solution B. Using A separation funnel, solution A is slowly added drop by drop to solution B in magnetic agitation to eventually form a blue-purple suspension. The suspension was left at room temperature for 24 hours, and then fully precipitated, washed with ethanol and deionized water several times, collected the precipitate, and then dried in the oven for 12 h to obtain the ZIF-67 (Co) sample.

S1.3. Synthesis of the MIL-101 (Fe)

At room temperature, 1 g ferric chloride ($FeCl_3 \cdot 6H_2O$) was dissolved in 60 ml DMF, fully stirred and dissolved, 0.306 g terephthalic acid ($C_9H_6O_6$) was added to the solution, and treated in ultrasonic water bath for 30 min to form a homogeneous orange transparent solution. The solution was transferred to a 100ml Teflon reactor and reacted

in an oven at 110 ° C for 24 hours. At the end of the reaction, the synthesized sample was washed several times with ethanol and deionized water, the washed solution was centrifuged, the precipitate was collected, and then dried in the oven for 12 h to obtain the MIL-101 (Fe) sample.

S1.4. Synthesis of the V-MOF

At room temperature, 0.8 g vanadium sulfate ($VOSO_4$) and 0.276 g 2-methylimidazole ($C_4H_6N_2$) was dissolved in 60 ml DMF, which was treated in an ultrasonic water bath for 30 min to form a uniform transparent solution. This solution was transferred to a 100ml teflon reactor and the solvent was thermally reacted in an oven at 160°C for 24 hours. After the reaction, the synthesized sample was washed three times with ethanol and deionized water, centrifuged to collect precipitation, and then dried in a vacuum drying oven for 12 h to obtain V-MOF.

S1.5. Synthesis of the MIL-101(Cr)

At room temperature, 1.42 g of chromium nitrate [$Cr(NO_3)_3 \cdot 6H_2O$] was dissolved in 50 ml DMF, fully agitated, and 0.418 g of terephthalic acid ($C_9H_6O_6$) was added to the solution, and was treated in an ultrasonic water bath for 30 min. The solution was transferred to a 100ml teflon reactor and reacted in an oven at 110°C for 24 hours. After the reaction, the synthesized sample was washed with ethanol and deionized water several times, centrifuged to collect precipitation, and then dried in a vacuum drying oven for 12 h to obtain dark green MIL-101 powder.

S1.6. Synthesis of the ZIF-8 (Zn)

At room temperature, dissolve 2.93 g $Zn(NO_3)_2 \cdot 6H_2O$ in 50ml methanol. Stir the solution until the zinc nitrate is completely dissolved to obtain the solution A. Dissolve 6.23 g 2-methylimidazole in 50 mL methanol. Stir the solution until the 2-methylimidazole is completely dissolved to obtain solution B. Pour solution A slowly into solution B, and stir constantly, the reaction produces a white precipitate. After

standing for 24 h, the solution was centrifuged, washed with DMF and deionized water, and dried in a vacuum drying oven for 12 h to obtain ZIF-8 (Zn).

S1.7. Alloy entropy calculation

The calculation of mixed entropy of high entropy alloys is based on the statistical mechanical definition of entropy. For a high entropy alloy containing n components, the mixing entropy ΔS_{mix} can be calculated using the following formula:

$$\Delta S_{mix} = -R\sum_{i=1}^{n} c_i Inc_i$$

Where R is the gas constant with a value of about 8.314 J/(mol·K). c_i is the mole fraction of the **i**th element. n is the number of elements in the alloy.

S1.8. EIS calculation model

The equivalent circuit is represented by Rs (R_1C_f) (R_2Q_{dl}), has a good tuning capability ($x^2<10^{-3}$), and is commonly used to fit impedance data for OER electrocatalytic processes. In an equivalent circuit, Rs represents the uncompensated solution resistance, R_1 represents the film resistance on the surface of the electrocatalyst, and C_f represents the corresponding capacitance. (R_1C_f) combination characterizes the physical response of the electrocatalyst interface in the middle and high frequency region in parallel. R_2 represents the charge transfer resistance in the electrochemical process, and Q_{dl} represents the corresponding capacitance. (R_2Q_{dl}) combines parallel OER processes corresponding to the low frequency region. The equivalent circuit diagram is as follows:

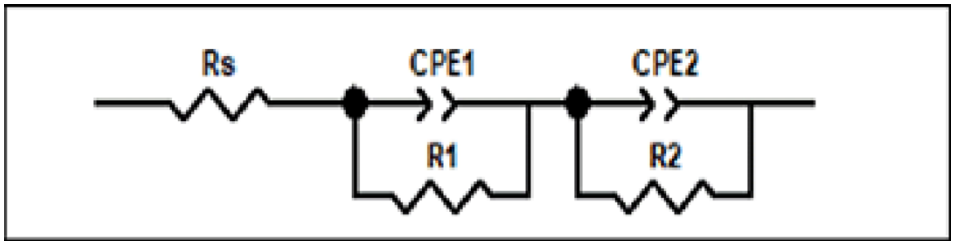

Considering the nonhomogeneity of the electrode surface, a constant phase element (CPE) is employed instead of the capacitive element (Q_{dl}), and the CPE impedance was represented by Equation:

$$Z_{CPE} = \frac{1}{Qdl(jw)^n} \quad (1)$$

where Q_{dl} refers to the mass factor in the double-layer capacitance, *n* is the corresponding dispersion coefficient (accounting for the deviation from the ideal behavior, the value being 1 for the perfect capacitors). *j* is the equivalent series

resistance of the capacitor and *w* is the angular frequency.

S1.9. Physical characterization

Scanning electron microscopy (SEM) images were obtained on Zeiss Sigma Scanning Electron Microscope. The high-resolution transmission electron microscopy (HRTEM), the corresponding selected area electron diffraction (SAED) and energy dispersive X-ray spectroscopy (EDX) results were measured on FEI Tecnai G2 F20 Field Emission Transmission Microscope. Powder X-ray diffraction (PXRD) Measurements were performed by a Rigaku Miniflex600 X-ray diffractometer with a Cu Kα radiation source (λ = 0.1542 nm) from 10 to 80° at the scan rate of 5°/min. N2 adsorption-desorption analysis was conducted on a Micromeritics ASAP 3020 instrument at 77 K. X-ray photoelectron spectroscopy (XPS) analyses were carried out by an X-ray photoelectron spectrometer (Thermo Fischer, ESCALAB Xi+) and the data was analyzed by CasaXPS Software version 2.3.19. In situ Raman spectra were collected with a Lab-RAM HR Evolutionary Raman spectrometer with a laser wavelength of 532 nm.

S1.10. Electrochemical measurements

All the electrochemical measurements were carried on a CHI-760E electrochemical workstation with a three-electrode system in 1M KOH, and the catalyst, Pt and Hg/HgO were chosen as working electrode, counter electrode and reference electrode, respectively. The catalyst ink was prepared by dispersing 3 mg catalyst in 1 mL Nafion solution (0.1 wt %) after 30 minutes ultrasonication. Before loading the catalyst, the surface of glassy carbon electrode (GCE, diameter 5 mm) was polished with 500 nm and 50 nm α-Al_2O_3 successively. After washed by ultrapure water and ethanol, 12 μL ink was dripped on the clean surface and dried at room temperature. The mass loading of catalyst was calculated as 0.3 mg cm^{-2}.

To remove the unstable parts and activate the catalysts, 200 cycle voltammetry scans (CVs) from the potential of 1.02 V to 1.82 V (vs. RHE) with a scan rate of 500 mV s^{-1} were taken prior to the Measurement. The OER cyclic voltammetry (CV) were Measured from the potential of 1.30 V to 1.77 V (vs. RHE) at the scan rate of 5 mV s^{-1}, and the polarization curves were determined by the negatively scan part of CV, the overpotentials (η) were obtained from: η = E (vs. RHE) -1.23 V. All the curves were recorded without iR correction.

The Tafel plots of catalysts were depicted from their corresponding linear sweep voltammograms (LSV) data, which can be fitted based on the equation below:

$$\eta = a + b \times log(j)$$

Where η is the overpotential, j is the steady-state current density to geometric area of working electrode. The durability test was performed using chronopotentiometry Measurements, and carbon rod was used as counter electrode to avoid Pt migration.

The electrochemical surface area (ECSA) was evaluated by CV technique from low range from 1.17 to 1.27 V (vs. RHE) under different scan rates from 10 to 50 mV s^{-1} to avoid the generation of Faradic current. The double-layer capacitance (C_{dl}) is linearly proportional to the ECSA, and it was estimated by plotting half of capacitive currents at 1.222 V (vs. RHE) ($\Delta J/2$, ΔJ equal to J_{anode} - $J_{cathode}$) against scan rate.

S1.11. DFT calculation model

In terms of computing in this work, first principles calculations are based on density functional theory (DFT) using the Vienna ab-initio simulation package (VASP), while Generalized Gradient Approximation (GGA) and Perdew-Burke-Ernzerhof (PBE) functionals are used to describe the exchange-related interaction terms. To reproduce the bulk properties, the atomic layer at the bottom is fixed.

Using Ni_3Fe and NiOOH as reference objects, we constructed the alloy (111) section of FeCoNiVCrZn alloy element and the composite M-OOH activation layer (100) section, and constructed a heterostructure with layer spacing of 3.17 Å and lattice index of 9.866 and 9.767 Å, respectively. Set the metal atom fraction occupancy ratio according to the element ratio obtained by EDS, and establish a vacuum layer greater than 15 Å along the z direction between the periodic images to avoid interference.

Ionic cores were described using projector-augmented wave (PAW) pseudo-potentials. The lowermost atomic layers were fixed in order to replicate the bulk characteristics. To characterize the van der Waals interaction, we applied the empirical adjustment found in Grimme's technique (DFT+D3). The energy and force convergence criteria are 10^{-6} eV and 5×10^{-2} eV, respectively. The cut-off energy of the plane wave base was set to 450 eV. The GGA + U method has not yet been applied in the present work.

S1.12. The reaction steps and calculation method of alkaline OER:

Based on the study of OER pathway in alkaline media, the OER pathway is generally described as a four-step reaction of continuous adsorption and desorption of the catalyst, and the related step reaction mechanism is shown in Eq (1) ~ Eq (4)

$$OH^- + M* \rightarrow M*OH + e^- \quad (1)$$

$$M*OH + H_2O \rightarrow M*O + OH^- + e^- \quad (2)$$

$$M*O + H_2O \rightarrow M*OOH + OH^- + e^- \quad (3)$$

$$M*OOH + OH^- \rightarrow M* + H_2O + O_2 + e^- \quad (4)$$

Among them, "M*" represents the active metal site in the catalyst, and the Fe,Co and Ni active sites of transition metals are mainly involved in this study. "M*OH" represents hydroxyl ions adsorbed at the active metal site, "M*OOH" represents peroxide groups adsorbed at the active metal site, and "M*O" represents oxygen ions adsorbed at the active metal site. To evaluate OER activity, the free energy (ΔG_1~ΔG_4) is calculated using the hydrogen electrode model of the calculation standard. The free energy is calculated as follows:

$$\Delta G_1 = G_{M*OH} - G_{M*} - G_{H2O} + 1/2G_{H2} - eU + K_B T\ln 10 \cdot pH \quad (5)$$

$$\Delta G_2 = G_{M*O} - G_{M*OH} + 1/2G_{H2} - eU + K_B T\ln 10 \cdot pH \quad (6)$$

$$\Delta G_3 = G_{M*OOH} - G_{M*O} - G_{H2O} + 1/2G_{H2} - eU + K_B T\ln 10 \cdot pH \quad (7)$$

$$\Delta G_4 = 4.92 - \Delta G_1 - \Delta G_2 - \Delta G_3 \quad (8)$$

Where K_B is the Boltzmann constant and -eU represents the change in free energy of an electron transfer, where U takes the electrode potential relative to the standard hydrogen electrode (vs SHE). For pH = 0, the effect of pH on the free energy can be defined as $-K_B T\ln 10 \cdot pH$, ΔG_4 is calculated using $4.92-\Delta G_1-\Delta G_2-\Delta G_3$ to avoid calculating adsorption and desorption of O_2.

S2. Figures and Tables

S2.1. Supplemental Figures

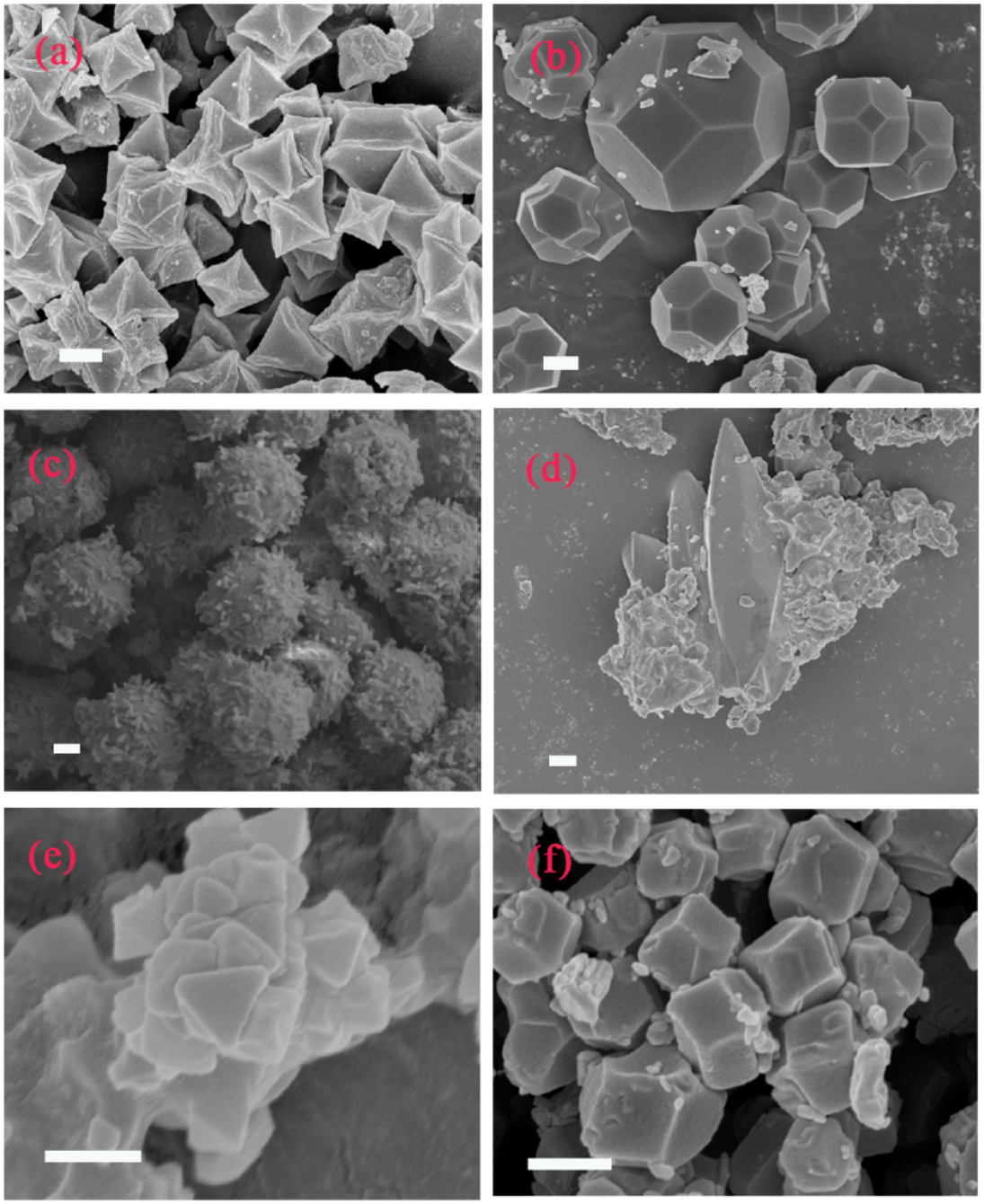

Figure S1. SEM images of a) MIL-101 (Fe), b) ZIF-67 (Co), c) Ni-MOF, d) V-MOF, e) MIL-101 (Cr) and f) ZIF-8 (Zn), scale bar equals to 500 nm.

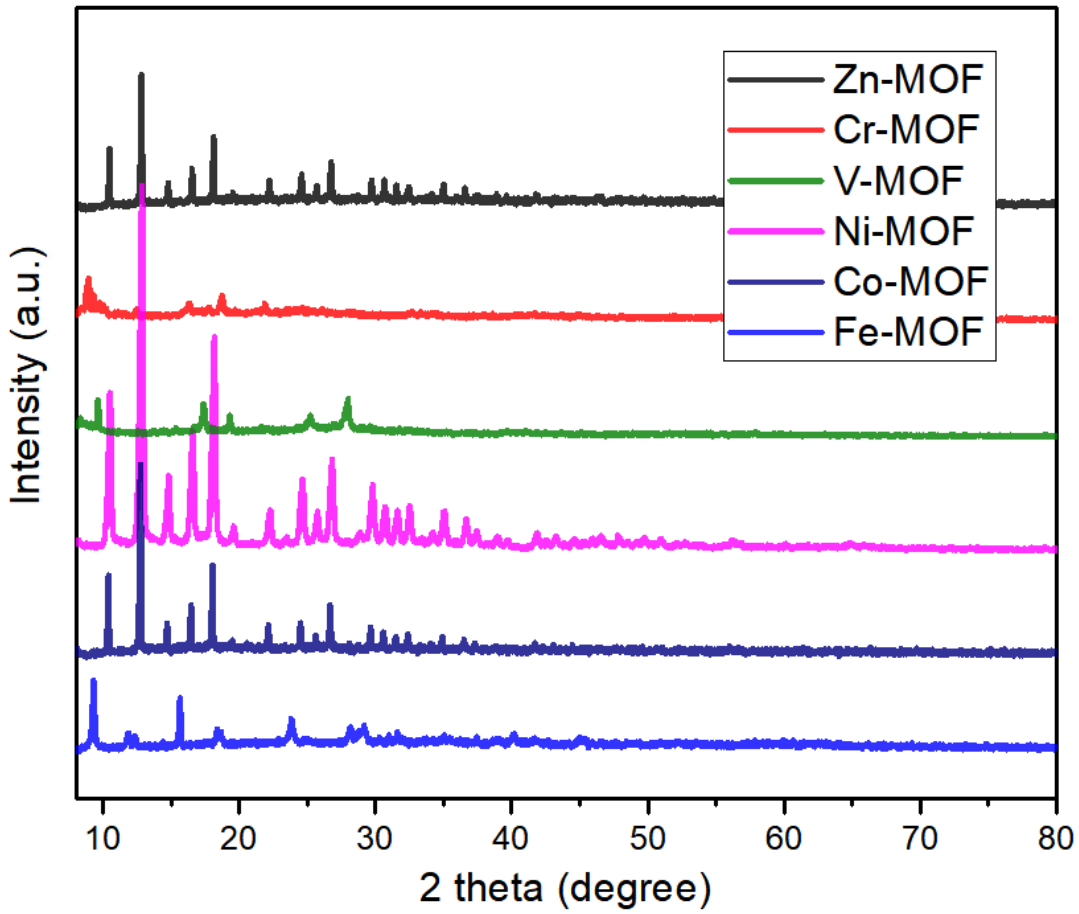

Figure S2. XRD patterns of MIL-101 (Fe), ZIF-67 (Co), Ni-MOF, V-MOF, MIL-101 (Cr) and ZIF-8 (Zn).

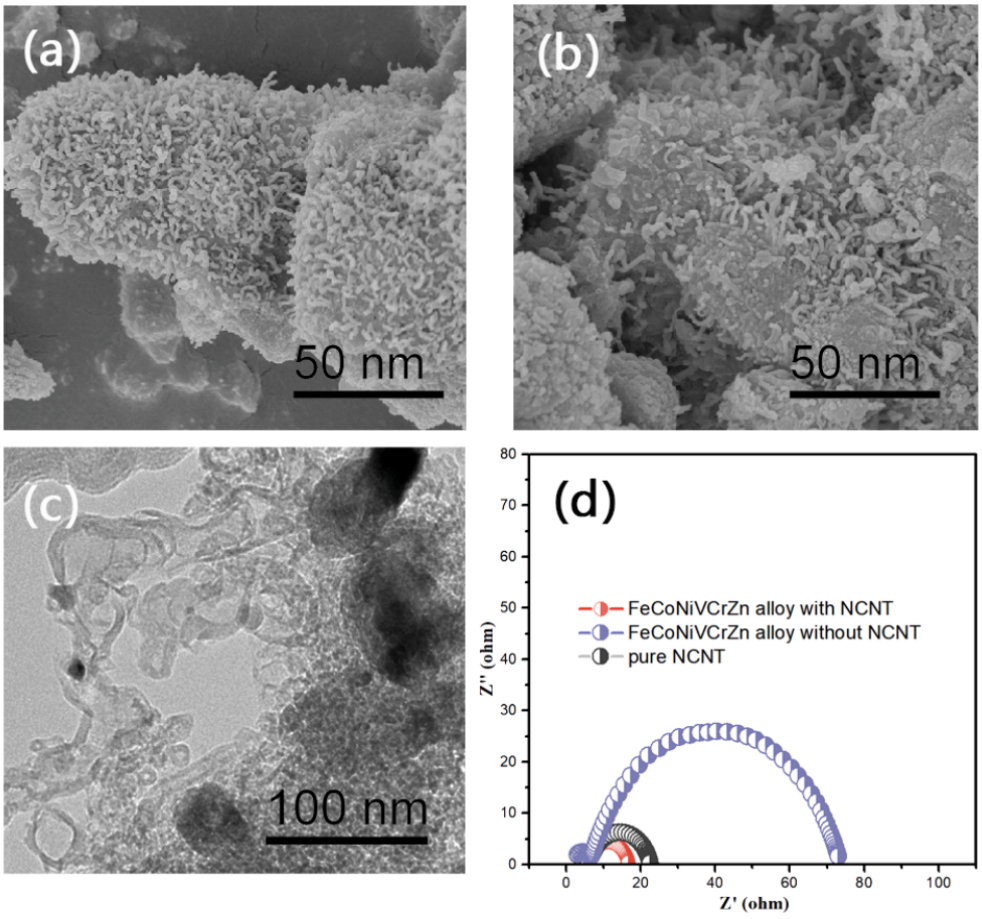

Figure S3. (a) SEM image of nitrogen-containing carbon nanotubes (NCNT) on the surface of FeCoNiVCrZn HEA catalyst; (b) SEM images of pure NCNT without metal composites; (c) TEM image of local NCNT of FeCoNiVCrZn HEA catalyst; (d) Comparison of Nyquist plots of FeCoNiVCrZn alloys with NCNT, FeCoNiVCrZn alloys without NCNT and pure NCNT materials, measured at 0.6 V versus Hg/HgO.

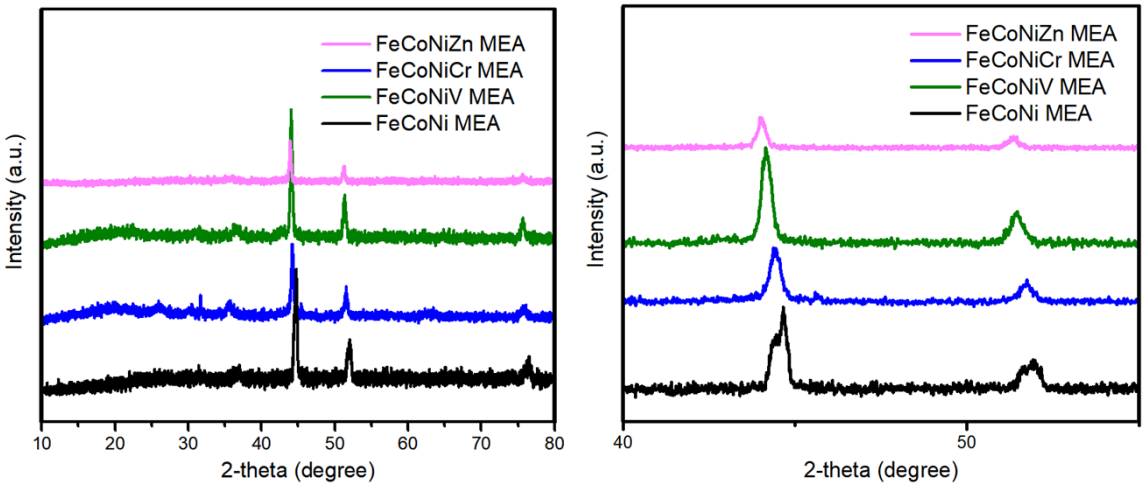

Figure S4. XRD patterns of a) FeCoNi trimetallic alloys and their derived four-metal alloys are combined with V, Cr and Zn, respectively. b) Close-up of local shift of characteristic diffraction peaks in Fig a.

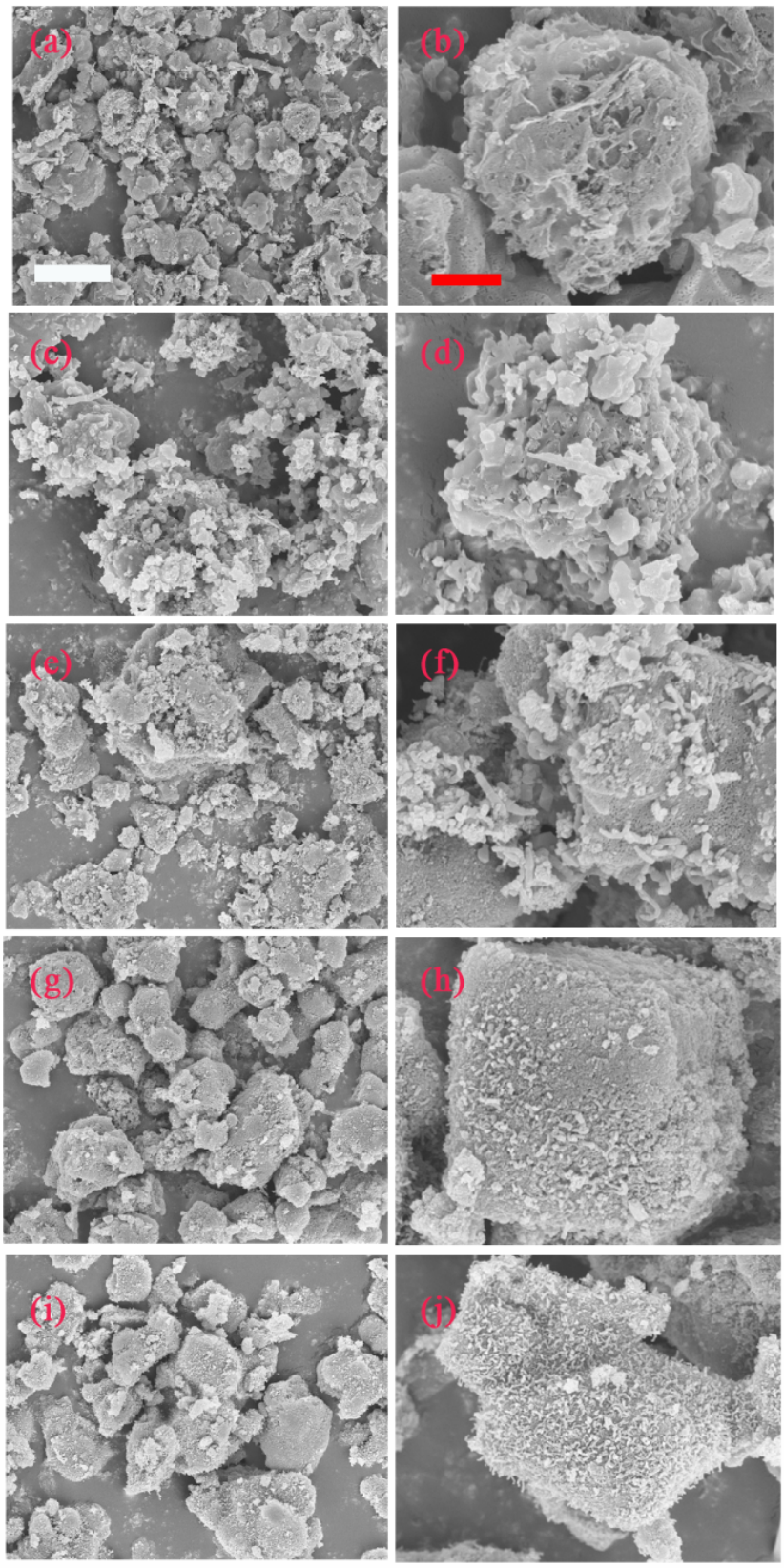

Figure S5. SEM images of a-b) FeCo LEA, c-d) FeCoNi MEA, e-f) FeCoNiV MEA, g-h) FeCoNiVCr HEA and i-j) FeCoNiVCrZn HEA. White scale bar equals to 2 µm and red scale bar equals to 500 nm

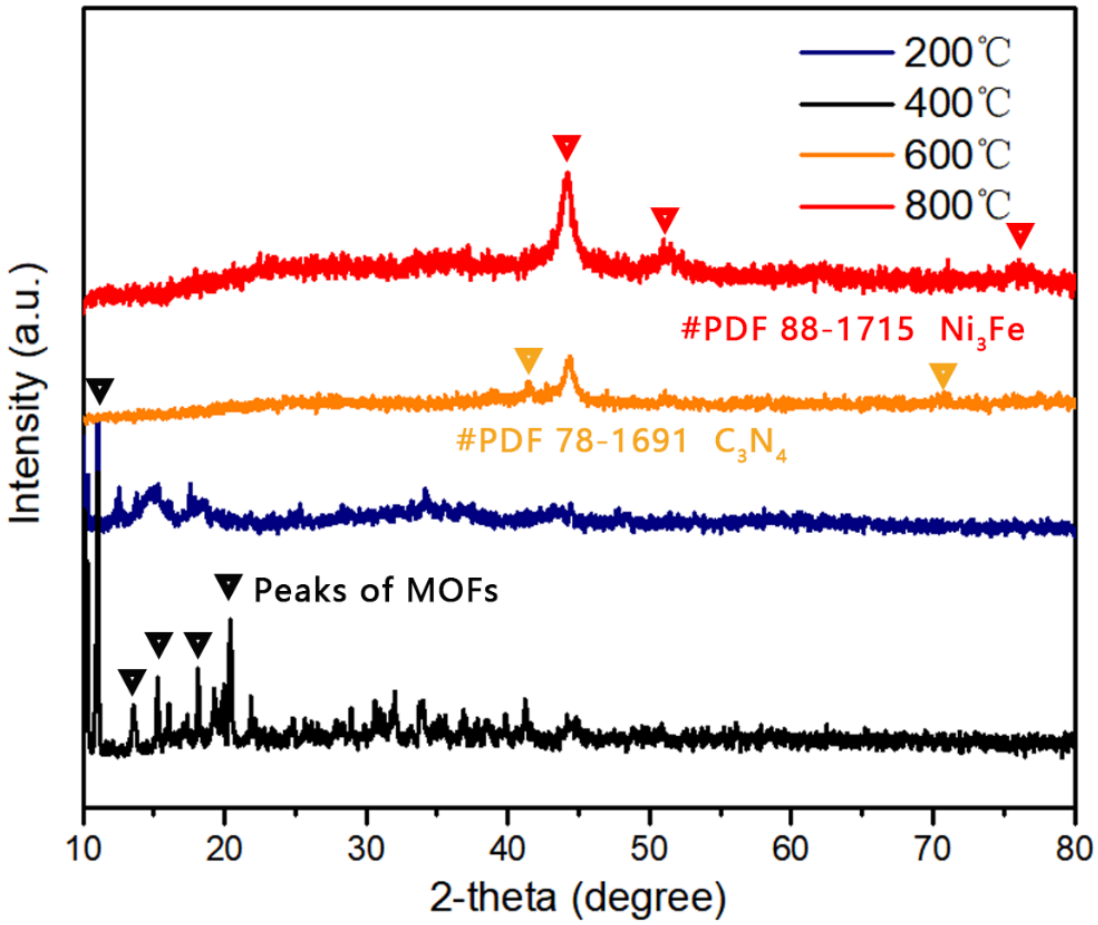

Figure S6. XRD patterns of products obtained by the pyrolysis of the MOFs-MA precursors at 200 -800℃.

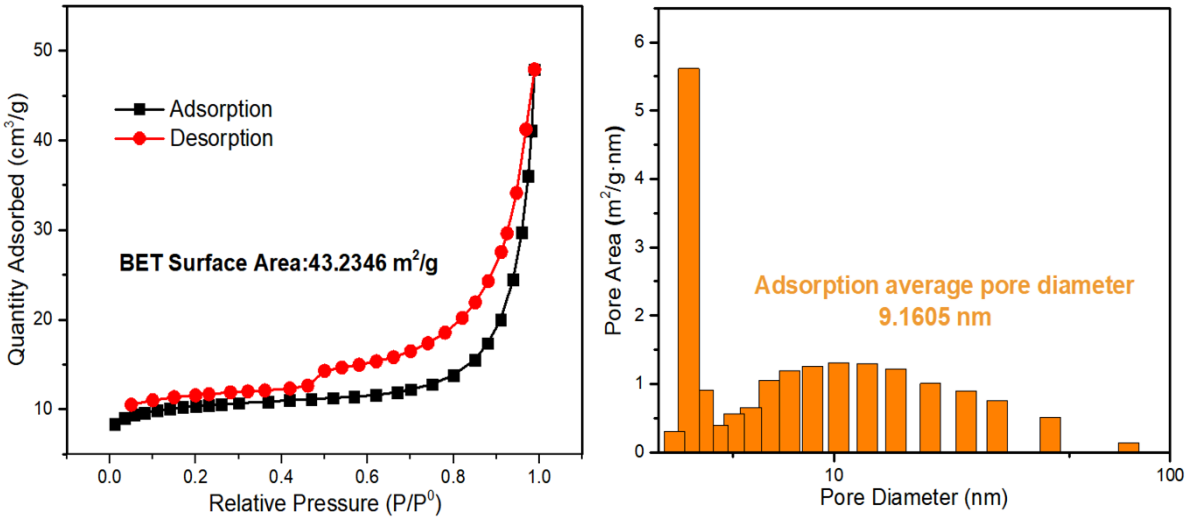

Figure S7. a) N_2 adsorption–desorption isotherms and b) pore size distribution histogram of FeCoNiVCrZn HEA.

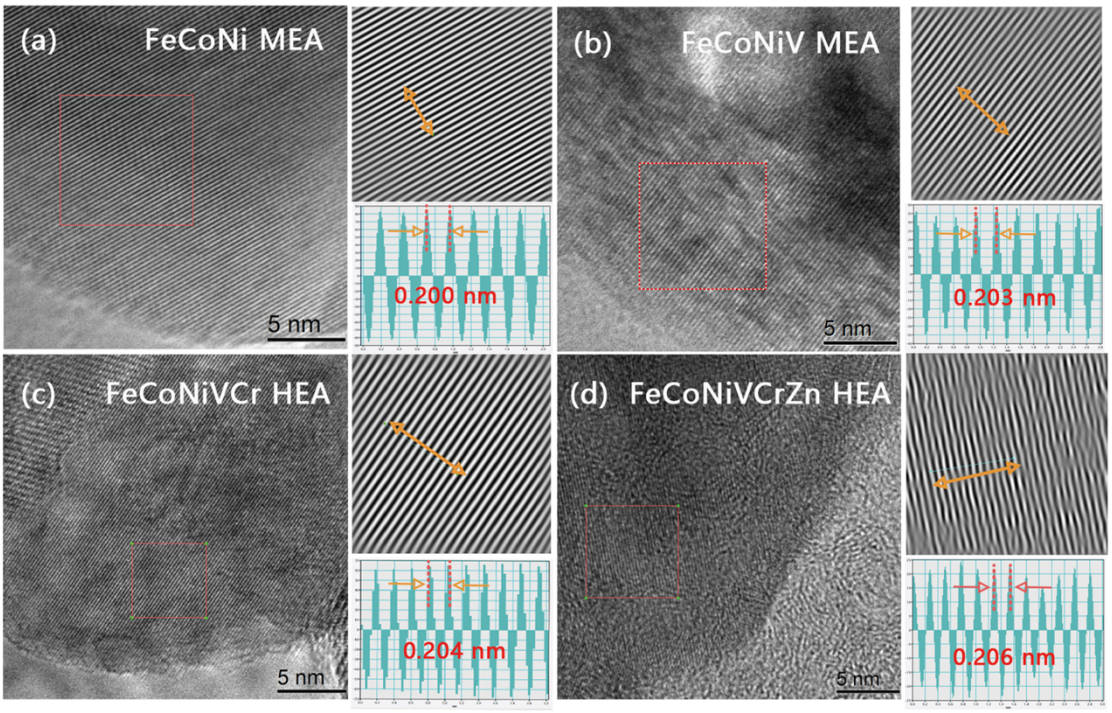

Figure S8. High-resolution TEM images, selected region FFT transform lattice fringe patterns and linear fringe intensity scanning of a) FeCoNi MEA, b) FeCoNiV MEA, c) FeCoNiVCr HEA and d) FeCoNiVCrZn HEA.

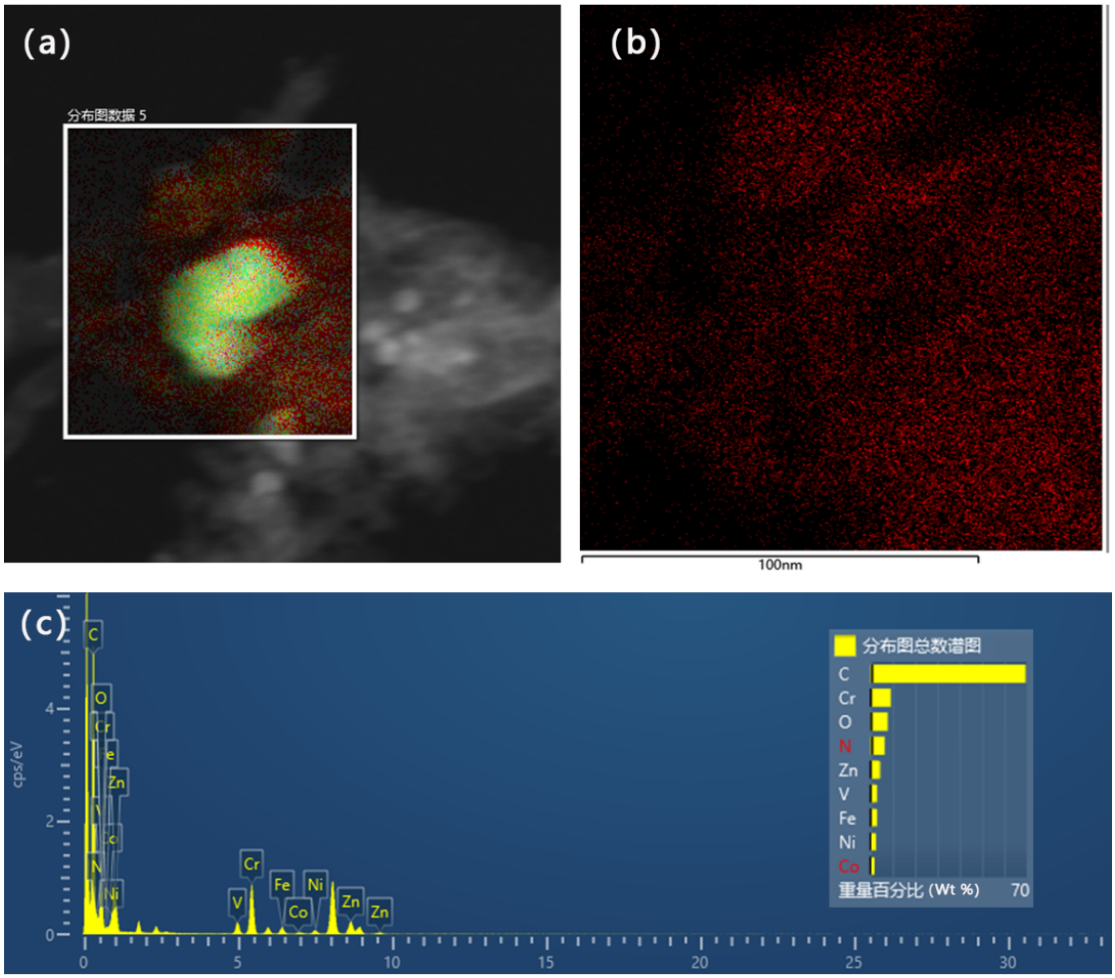

Figure S9. Supplement to The EDS picture in Fig. 2j in the manuscript. (a) the element map signal mixing mapping; (b) Carbon element distribution of carbon-coated matrix and carbon nanotubes in FeCoNiVCrZn HEA; (c) FeCoNiVCrZn HEA surface element total response signal distribution energy spectrum.

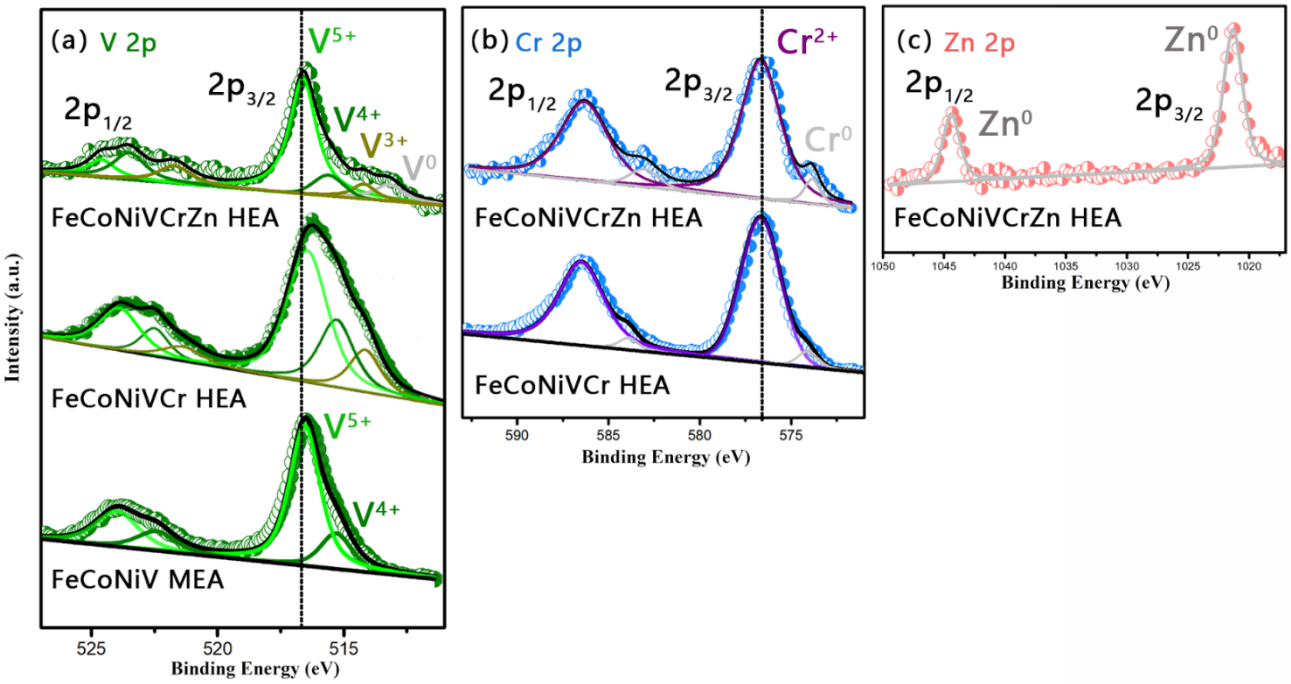

Figure S10. Energy spectrum of the overall mass distribution of the surface elements of FeCoNiVCrZn HEA.

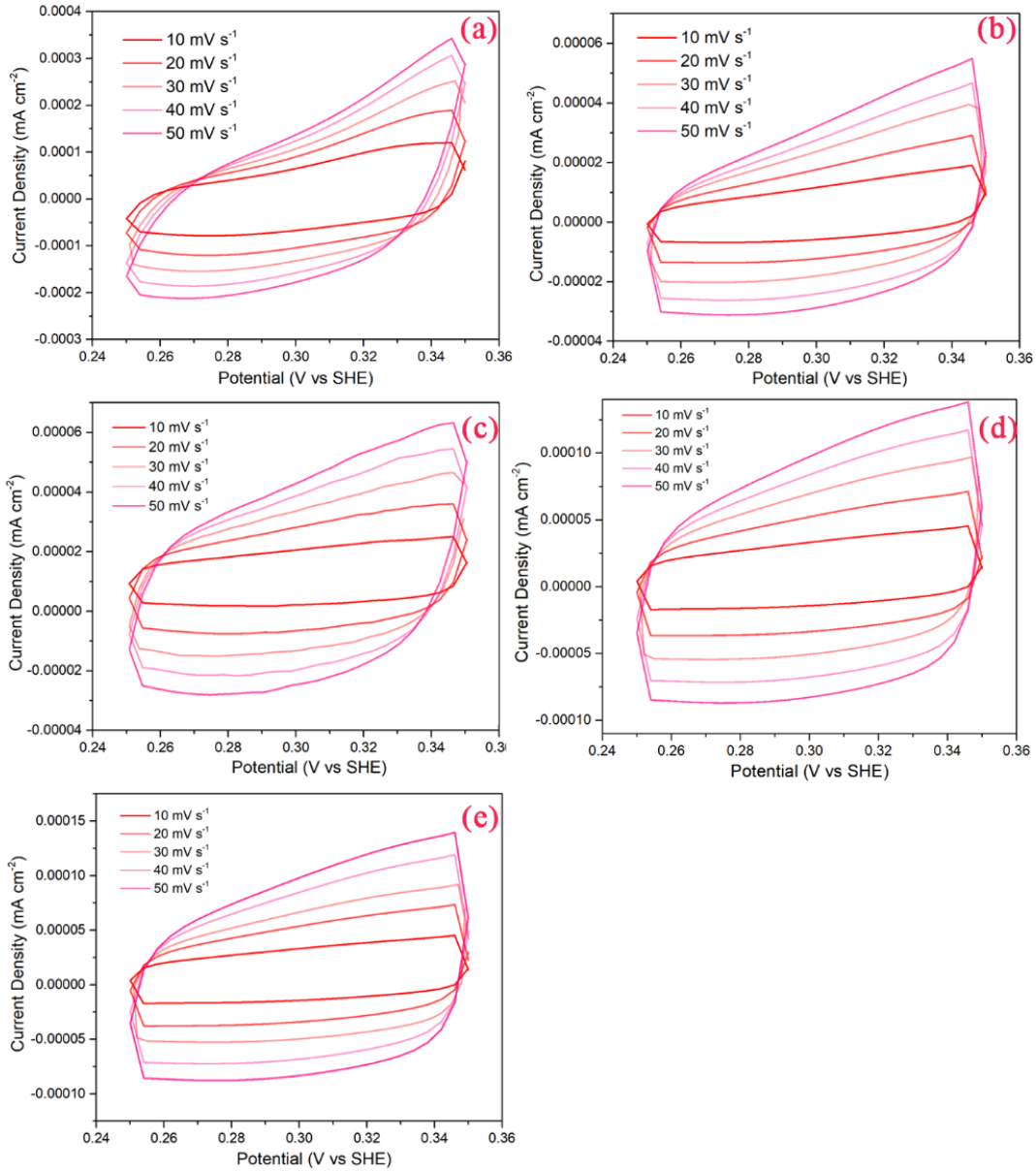

Figure S11. Electrochemical cyclic voltammetry scans recorded for a) FeCoNiVCrZn HEA, b) FeCoNiVCr HEA, c) commercial IrO_2/C, d) FeCoNiV MEA and e) FeCoNi MEA. Scan rates are 10, 20, 30, 40 and 50 mV s^{-1}.

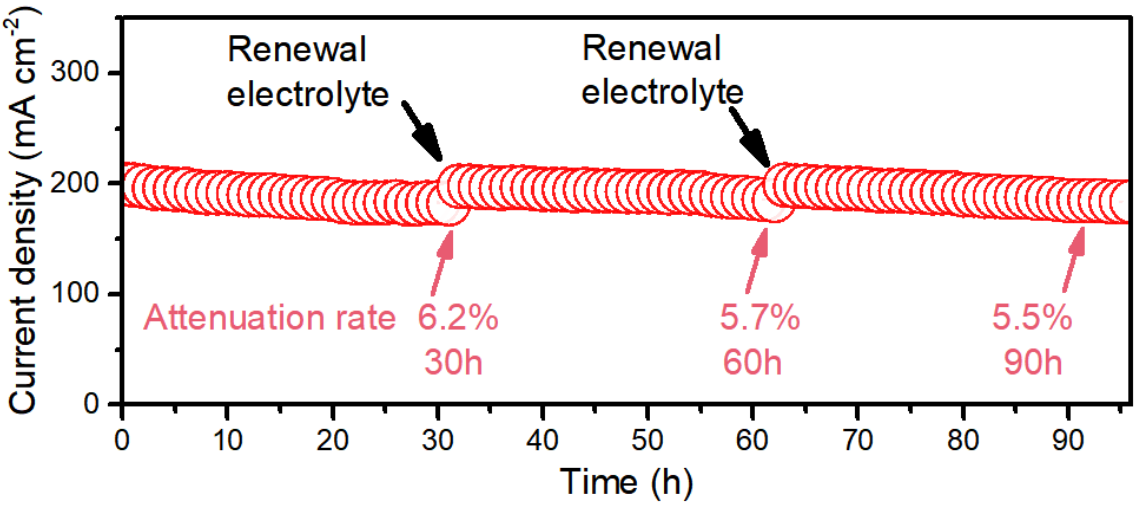

Figure S12. Chronoamperometry curve of FeCoNiVCrZn HEA under large current density (~200mA cm^{-2}) provided by 2V DC power supply.

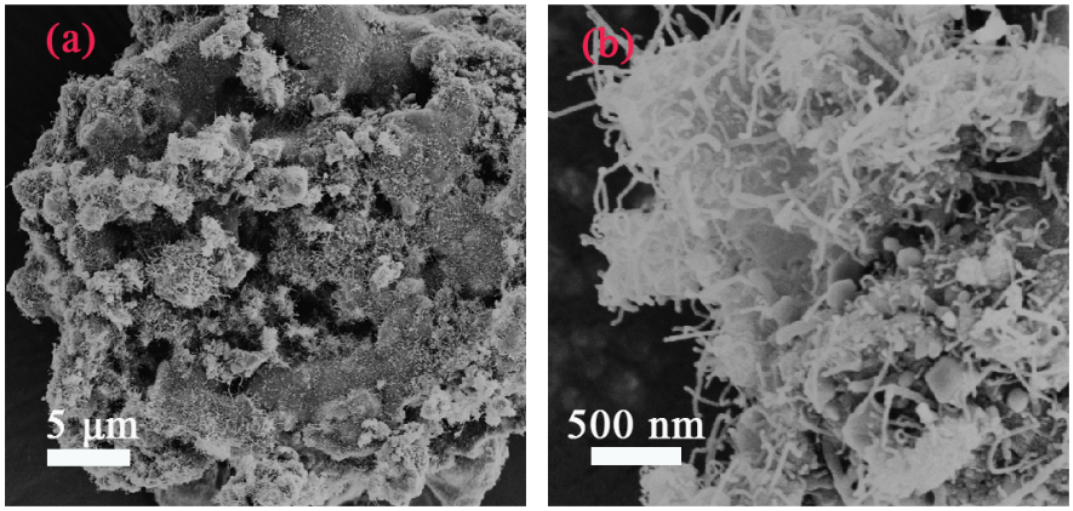

Figure S13. SEM images of the FeCoNiVCrZn HEA catalyst after 3000th CV cycle in 1.0M KOH.

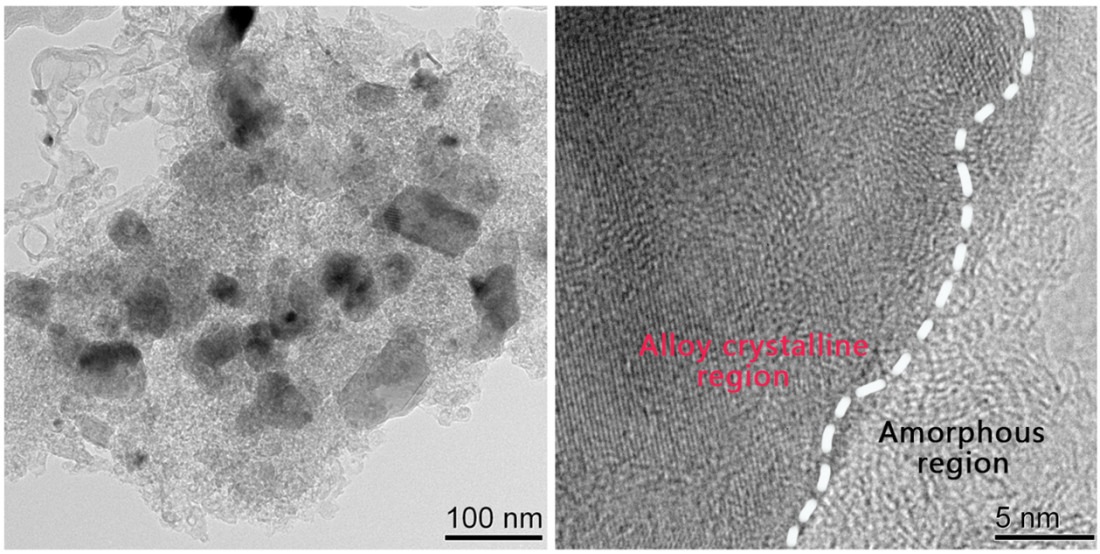

Figure S14. TEM images of the FeCoNiVCrZn HEA catalyst after 3000th CV cycle in 1.0M KOH. a) the catalyst as a whole, including alloy particles and nitrogen-containing carbon nanotubes, b) high entropy alloy particles crystal and amorphous interface close-up.

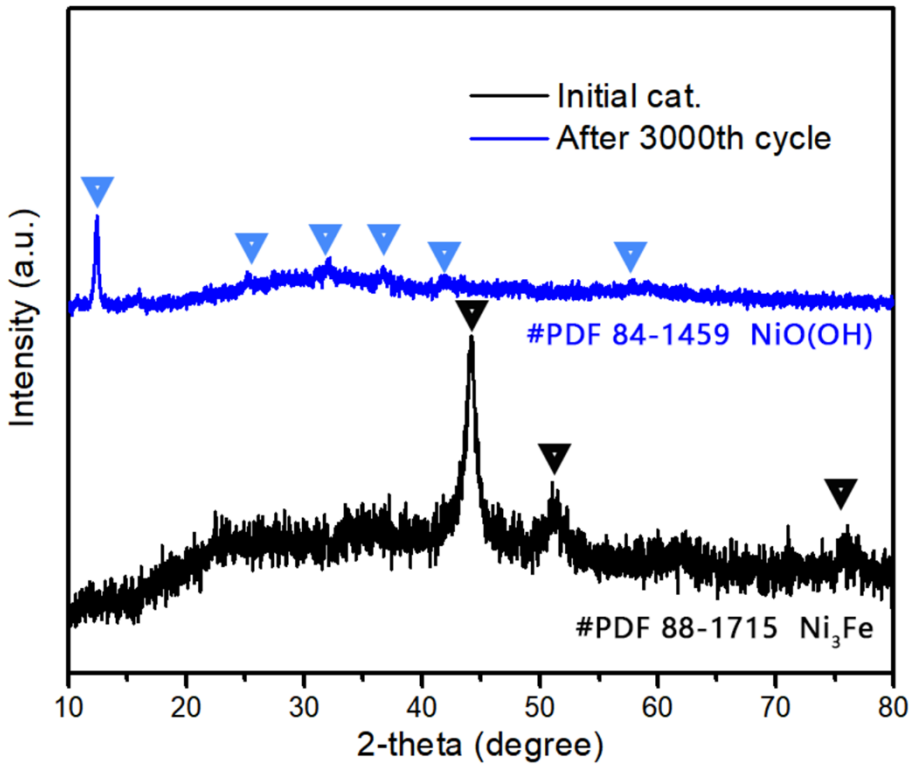

Figure S15. Comparative XRD pattern of the FeCoNiVCrZn HEA catalyst after undergoing a 3000th CV cycles in 1.0M KOH.

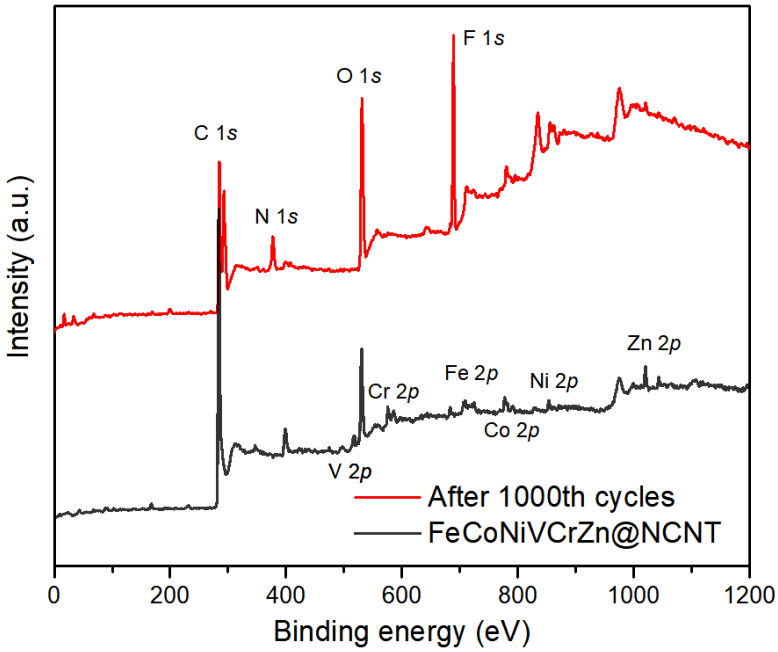

Figure S16. Comparative XRD pattern of the FeCoNiVCrZn HEA catalyst after undergoing a 3000th CV cycles in 1.0M KOH. XPS

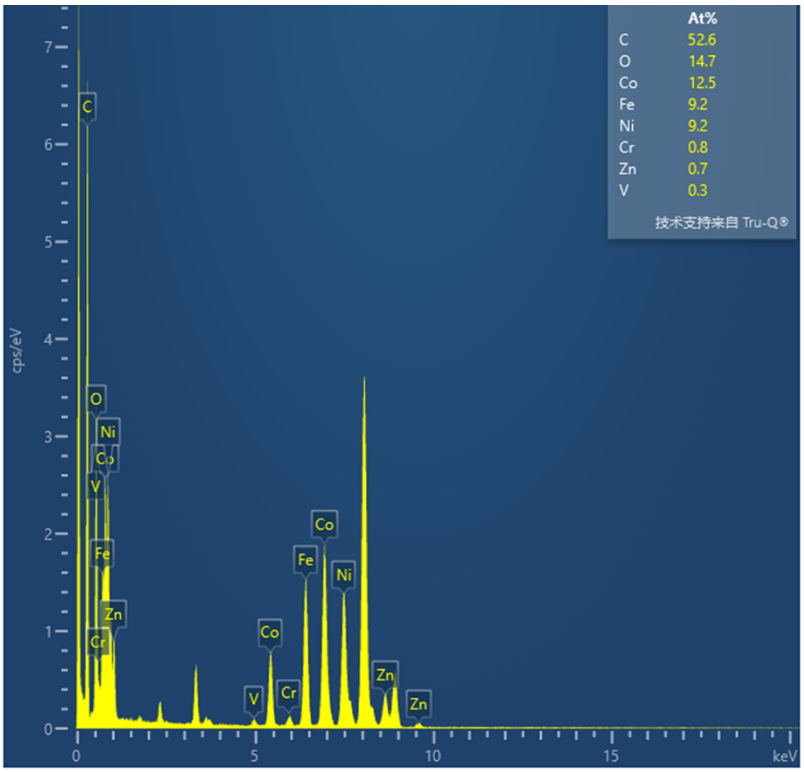

Figure S17. Energy spectrum of the overall mass distribution of the surface elements of FeCoNiVCrZn HEA after undergoing a 3000th CV cycles in 1.0M KOH.

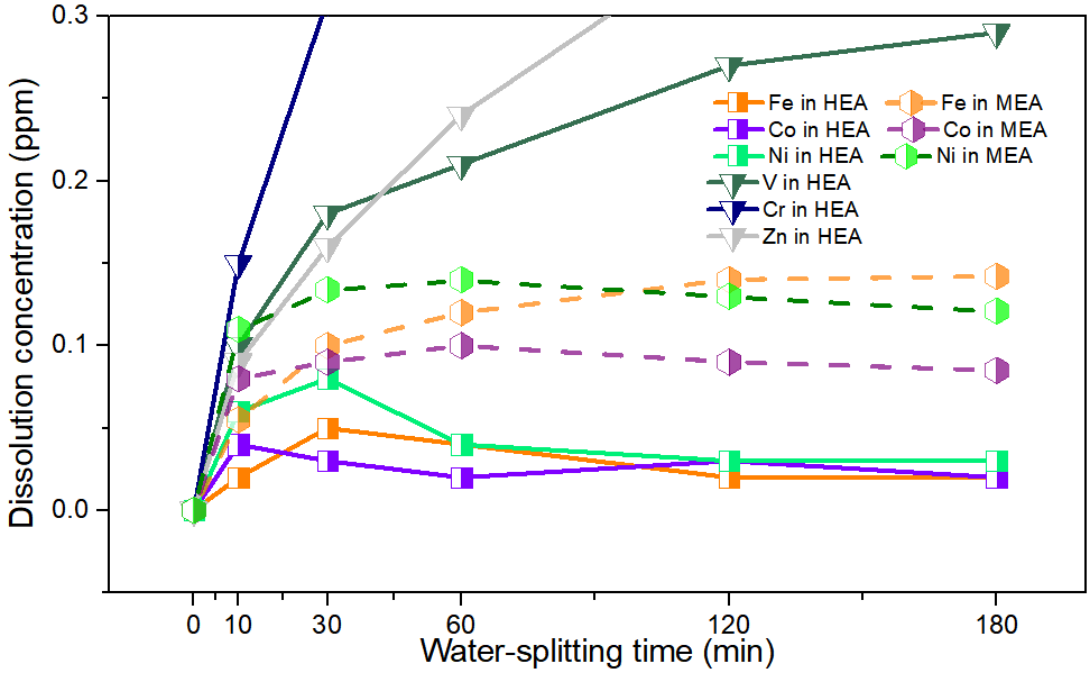

Figure S18. Curve diagram of the concentration of dissolved metal ions (ppm) in the electrolyte of FeCoNiVCrZn HEA and FeCoNi MEA loaded on the carbon cloth carrier under constant current of 10 mA cm^{-2} (Regular sampling from electrolyte for ICP-OES test).

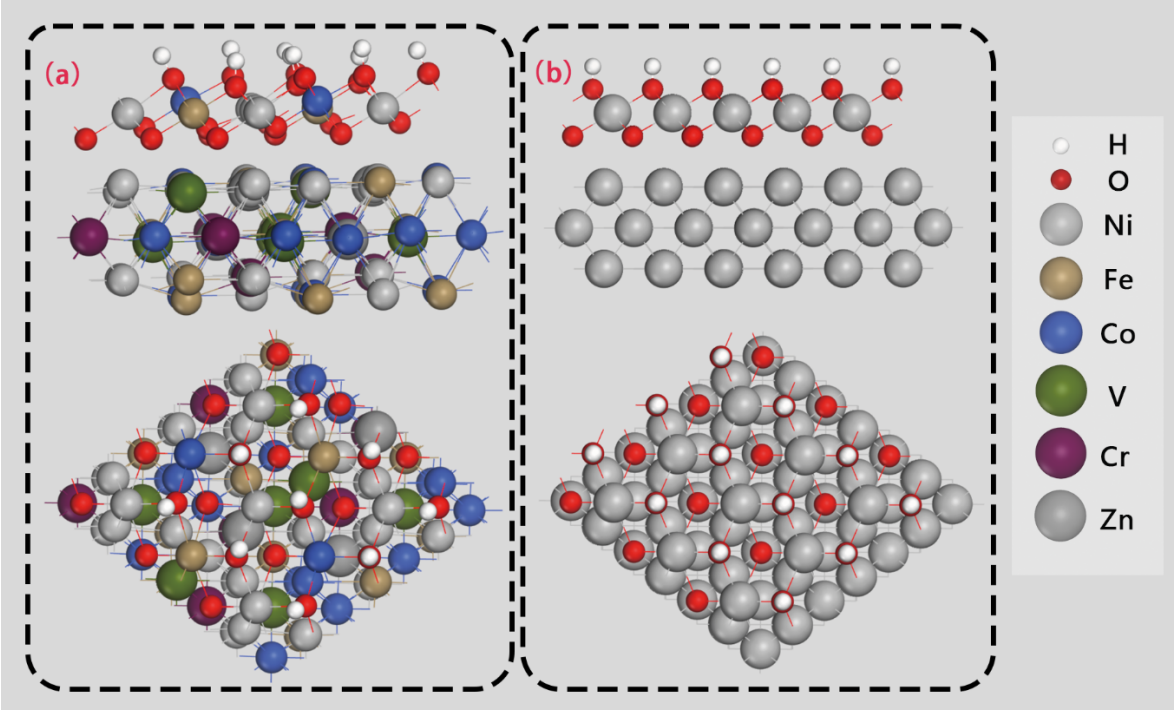

Figure S19. The top view and the side view of a) the heterojunction between FeCoNiVCrZn (111) crystal face and FeCoNi-OOH (100) crystal face and b) the heterojunction between Ni (111) crystal face and NiOOH (100) crystal face.

S3.2. Supplemental Tables

Table S1. The metals atomic mass composition (w %) of samples determined by ICP-OES.

sample	Fe	Co	Ni	V	Cr	Zn
FeCoNiVCrZn HEA	15.41	23.63	23.03	13.21	14.88	9.83
FeCoNiVCr HEA	16.53	24.61	24.08	15.51	15.27	--
FeCoNiV MEA	21.08	30.43	31.33	17.16	--	--
FeCoNi MEA	23.65	41.36	34.99	--	--	--
FeCo LEA	42.10	57.90	--	--	--	--

Table S2. Lorentz fitting results of (100) crystal face main peaks for homogeneous alloys FeCoNi, FeCoNiV, FeCoNiVCr and FeCoNiVCrZn. The corresponding 2-theta, FWHM values, grain size (D) and lattice spacing (d) as determined by the Scheller's equation (Eq.9) and the Bragg formula(Eq.10) .

$D = K\lambda / (\beta\cos\theta)$ (9)

$2d\sin\theta = n\lambda$ (10)

sample	2θ/°	FWHM/°	D/Å	$d_{(111)}$/Å
FeCoNiVCrZn HEA	42.9	1.33	2.121	2.045
FeCoNiVCr HEA	43.3	1.18	2.032	1.994
FeCoNiV MEA	43.7	0.84	2.005	1.981
FeCoNi MEA	43.5	0.95	1.920	1.850

Table S3. The surface atomic composition (%) of samples determined by XPS.

sample	Fe	Co	Ni	V	Cr	Zn
FeCoNiVCrZn HEA	12.58	25.70	28.89	8.96	13.99	9.88
FeCoNiVCr HEA	14.53	28.69	30.31	10.26	16.21	--
FeCoNiV MEA	20.45	33.50	34.33	11.72	--	--
FeCoNi MEA	25.78	37.65	36.57	--	--	--
FeCo LEA	45.92	54.08	--	--	--	--

Table S4. The concentration of dissolved metal ions (ppm) in the FeCoNiVCrZn HEA catalyst electrolyte recorded by ICP-OES during the OER process changes with time.

Time (min)	Fe	Co	Ni	V	Cr	Zn
0	0.00	0.00	0.00	0.00	0.00	0.00
10	0.02	0.04	0.06	0.10	0.15	0.09
30	0.05	0.03	0.08	0.18	0.31	0.16
60	0.04	0.02	0.04	0.21	0.37	0.24
120	0.02	0.03	0.03	0.27	0.42	0.35
180	0.02	0.02	0.03	0.29	0.43	0.37

Table S5. Metal element content changes of FeCoNiVCrZn @ NCNT catalyst after 1000 CV cycles, determined by ICP-OES (w%)and XPS (atomic %) for the whole and surface locally.

Metal Element		**Fe**	**Co**	**Ni**	**V**	**Cr**	**Zn**
Before 1000th CV cycles	ICP-OES	15.41	23.63	23.03	13.21	14.88	9.83
	XPS	12.58	25.70	28.89	8.96	13.99	9.88
After 1000th CV cycles	ICP-OES	19.71	28.62	25.75	5.92	12.33	7.67
	XPS	27.61	37.79	33.19	0.40	0.88	0.13

Table S6. Comparison of OER activity of FeCoNiVCrZn HEA in this work with other reported electrocatalysts in 1 M alkaline solution.

Catalysts	η_{10}(mV)	Tafel slope (mV dec^{-1})	Ref.
FeCoNiVCrZn HEA	249	50	This work
FeCoNiMnCuBOy	259	66.1	[1]
CoNi-CoN_3/C	360	134.7	[2]
FeCoNiMnCu HEA	280	59	[3]
$Fe_{0.5}CoNiCuZn_{0.8}$ HEA	340	48	[4]
FeNiPt@C NFs	294	67	[5]
β -FeCo-PCNF	265	116	[6]
FeNi@C(N_{10})	326	50	[7]
$Mg_{0.2}Co_{0.2}Ni_{0.2}Cu_{0.2}Zn_{0.2}O$	360	61.4	[8]
$Ni_{40}Fe_{40}B_{20}$	319	56	[9]
AlNiCoRuMo	270	54.5	[10]
RhRuFe TMs/C	330	64.5	[11]
H-$CoTe_2$/$NiTe_2$@NCBs	320	64.8	[12]
$LaNi_{0.1}Fe_{0.9}O_3$	350	73	[13]

Uncategorized References

1. S. Jiang, Y. Yu, H. He, Z. Wang, R. Zheng, H. Sun, Y. Liu and D. Wang, General Synthesis of Composition‐Tunable High‐Entropy Amorphous Oxides Toward High Efficiency Oxygen Evolution Reaction, *Small*, 2024, DOI: 10.1002/smll.202310786.
2. N. Li, M. Sun, J. Xiao, X. Ma, L. Huang, H. Li, C. Xie, Y. Yang, H. Jiang, B. Huang and W. Zhang, Highly Active CoNi‐CoN3 Composite Sites Synergistically Accelerate Oxygen Electrode Reactions in Rechargeable Zinc–Air Batteries, *Small*, 2024, DOI: 10.1002/smll.202401506.
3. K. Huang, D. Peng, Z. Yao, J. Xia, B. Zhang, H. Liu, Z. Chen, F. Wu, J. Wu and Y. Huang, Cathodic plasma driven self-assembly of HEAs dendrites by pure single FCC FeCoNiMnCu nanoparticles as high efficient electrocatalysts for OER, *Chem. Eng. J.*, 2021, **425**.
4. J. Huang, P. Wang, P. Li, H. Yin and D. Wang, Regulating electrolytic Fe0.5CoNiCuZn high entropy alloy electrodes for oxygen evolution reactions in alkaline solution, *Journal of Materials Science & Technology*, 2021, **93**, 110-118.
5. Y. Pan, Y. Li, A. Nairan, U. Khan, Y. Hu, B. Wu, L. Sun, L. Zeng and J. Gao, Constructing FeNiPt@C Trifunctional Catalyst by High Spin‐Induced Water Oxidation Activity for Zn‐Air Battery and Anion Exchange Membrane Water Electrolyzer, *Adv. Sci.*, 2024, **11**.
6. P. Li, F. Qiang, X. Tan, Z. Li, J. Shi, S. Liu, M. Huang, J. Chen, W. Tian, J. Wu, W. Hu and H. Wang, Electronic modulation induced by decorating single-atomic Fe-Co pairs with Fe-Co alloy clusters toward enhanced ORR/OER activity, *Appl. Catal. B-Environ.*, 2024, **340**.
7. W. Miao, X. Cao, M. Qin, E. Lv, H. Yu, X. Zhang and X. Dong, N-doping FeNi@C(Nx) core-shell nanoparticles synthesized by arc plasma as a highly efficient bifunctional electrocatalyst for all-solid zinc-air batteries, *Composites, Part B*, 2023, **260**.
8. F. Liu, M. Yu, X. Chen, J. Li, H. Liu and F. Cheng, Defective high-entropy rocksalt oxide with enhanced metal–oxygen covalency for electrocatalytic oxygen evolution, *Chin. J. Catal.*, 2022, **43**, 122-129.
9. H.-l. Li, Y.-y. Wang, C.-m. Liu, S.-m. Zhang, H.-f. Zhang and Z.-w. Zhu, Enhanced OER performance of NiFeB amorphous alloys by surface self-reconstruction, *Int. J. Hydrogen Energy*, 2022, **47**, 20718-20728.
10. Z. Jin, J. Lyu, Y.-L. Zhao, H. Li, X. Lin, G. Xie, X. Liu, J.-J. Kai and H.-J. Qiu, Rugged High-Entropy Alloy Nanowires with in Situ Formed Surface Spinel Oxide As Highly Stable Electrocatalyst in Zn–Air Batteries, *ACS Mater. Lett.*, 2020, **2**, 1698-1706.
11. W. Zhang, K. Wang, F. Lin, Q. Zhang, Y. Sun, H. Luo, W. Zhang, J. Zhou, F. Lv, D. Wang, L. Gu, M. Luo and S. Guo, Assembled RhRuFe Trimetallene for Water Electrolysis, *Small Methods*, 2024, DOI: 10.1002/smtd.202400336.
12. M. Liu, Q. Li, X. Xiao, X. Ma, X. Xu, Y. Yin, B. Zhang, M. Ding, J. Zou and B. Jiang, CoTe2/NiTe2 heterojunction embedded in N-doped hollow carbon nanoboxes as high-efficient ORR/OER catalyst for rechargeable zinc-air battery, *Chem. Eng. J.*, 2024, **486**.
13. H. Cheraparambil, M. Vega-Paredes, C. Scheu and C. Weidenthaler, Unraveling the Evolution of Dynamic Active Sites of LaNixFe1–xO3 Catalysts During OER, *ACS Appl. Mater. Interfaces*, 2024, **16**, 21997-22006.